Journal of Power Sources 196 (2011) 255–263

Contents lists available at ScienceDirect

Journal of Power Sources

journal homepage: www.elsevier.com/locate/jpowsour

Modeling hydrogen starvation conditions in proton-exchange membrane fuel cells

Jan Hendrik Ohs[a,*], Ulrich Sauter[a], Sebastian Maass[a], Detlef Stolten[b]

[a] Robert Bosch GmbH, Robert-Bosch-Platz 1, 70839 Gerlingen-Schillerhöhe, Germany
[b] Forschungszentrum Jülich GmbH, IEF-3: Fuel Cells, 52425 Jülich, Germany

ARTICLE INFO

Article history:
Received 27 April 2010
Received in revised form 8 June 2010
Accepted 11 June 2010
Available online 31 July 2010

Keywords:
PEMFC modeling
Cell degradation
Carbon corrosion
Reverse current decay mechanism
Agglomerate model

ABSTRACT

In this study, a steady state and isothermal 2D-PEM fuel cell model is presented. By simulation of a single cell along the channel and in through-plane direction, its behaviour under hydrogen starvation due to nitrogen dilution is analysed. Under these conditions, carbon corrosion and water electrolysis are observed on the cathode side. This phenomenon, causing severe cell degradation, is known as reverse current decay mechanism in literature. Butler–Volmer equations are used to model the electrochemical reactions. In addition, we account for permeation of gases through the membrane and for the local water content within the membrane. The results show that the membrane potential locally drops in areas starved from hydrogen. This leads to potential gradients >1.2 V between electrode and membrane on the cathode side resulting in significant carbon corrosion and electrolysis reaction rates. The model enables the analysis of sub-stoichiometric states occurring during anode gas recirculation or load transients.

1. Introduction

Fuel cells are a promising technology for clean and efficient energy conversion. For automotive applications, proton-exchange membrane fuel cells (PEMFC) are the preferred type due to their low operating temperature ($T < 120\,^{\circ}C$) and dynamic behaviour. One of the main challenges for developing a commercial PEMFC system, competitive with the combustion engine, is the limited long term stability.

Under fuel cell operation, hydrogen is oxidised and oxygen is reduced in the anode and cathode catalyst layer, respectively (all standard potentials φ_{00} are given in [1]):

$$2\,H^+ + 2\,e^- \rightleftarrows H_2 \qquad \varphi_{00} = 0\,V \tag{1}$$

$$O_2 + 4\,H^+ + 4\,e^- \rightleftarrows 2\,H_2O \qquad \varphi_{00} = 1.23\,V \tag{2}$$

In total, electric energy, water and heat are produced. In addition to hydrogen oxidation and oxygen reduction, there are undesired side reactions causing irreversible cell degradation and therefore limiting the long-term stability of the system. Carbon corrosion (Eq. (3)), water electrolysis (the back reaction of Eq. (2)) and platinum dissolution (Eq. (4)) are the main undesired side reactions in PEMFCs:

$$CO_2 + 4\,H^+ + 4\,e^- \rightleftarrows C + 2\,H_2O \qquad \varphi_{00} = 0.2\,V \tag{3}$$

$$Pt^{2+} + 2\,e^- \rightleftarrows Pt \qquad \varphi_{00} = 1.19\,V \tag{4}$$

Typical cathode potentials are in a range of $\varphi_C = 0.5\,V, \ldots, 1\,V$ vs. RHE. Thus, it can be seen from Eq. (3) that carbon is thermodynamically unstable under standard operating conditions. Fortunately, the reaction is kinetically hindered and corrosion reaction rates are negligible for a cell voltage $U_{cell} < 1\,V$ and temperature $T < 120\,^{\circ}C$ [2]. Water electrolysis is not relevant at standard conditions due to its high equilibrium potential. Platinum dissolution is observed at standard conditions particularly under dynamic potential cycling operation mode [7]. According to the Pourbaix-diagram [4], platinum can be dissolved at $\varphi < 1\,V (pH \approx 0)$ if the Pt^{2+}-concentration in solution is very low.

A cell that is locally starved of hydrogen in the rear part of the anode (Fig. 1) shows severe carbon corrosion in the experiments [2]. Reiser et al. propose the reverse current decay (RCD) mechanism which leads to high cathode potentials ($\varphi_C > 1\,V$) in the hydrogen starved part of the cell.

Locally starved conditions occur during startup when a H_2 / O_2-front is moving through the cell within milliseconds and during steady states when the cell is operated sub-stoichiometrically, for example if a fuel channel is blocked by impurities or liquid water. In the latter case, oxygen is available in the H_2-starved regions of the anode catalyst layer due to permeation through the membrane. During RCD-operation, the front part of the cell acts as a

* Corresponding author. Tel.: +49 711 811 7182; fax: +49 711 811 5180111.
E-mail address: janhendrik.ohs@de.bosch.com (J.H. Ohs).

0378-7753/$ – see front matter © 2010 Elsevier B.V. All rights reserved.
doi:10.1016/j.jpowsour.2010.06.038

Nomenclature

a	water activity
A	active surface area per volume unit of catalyst layer (m^{-1})
c	concentration ($mol\,m^{-3}$)
D	diffusion coefficient ($m^2\,s^{-1}$)
$\tilde{D}_{i,k}$	Maxwell–Stefan diffusion coefficient matrix ($m^2\,s^{-1}$)
E	activation energy ($kJ\,mol^{-1}$)
f	volume fraction of water in membrane
F	Faraday constant ($C\,mol^{-1}$)
i	current density ($A\,m^{-3}$)
i^0	exchange current density ($A\,m^{-3}$)
k	reaction constant (s^{-1})
k_i	parameter
M_T	Thiele-Modulus
n	electrons involved in electrochemical reaction
N	flux density ($mol\,m^{-2}\,s^{-1}$)
p	pressure (Pa)
p_i	partial pressure of component i (Pa)
rH	relative humidity
R_i	source term ($kg\,m^{-3}\,s^{-1}$)
R_{agg}	agglomerate radius (m)
R	ideal gas constant ($J\,mol^{-1}\,K^{-1}$)
T	temperature (K)
$\bar{u}$	velocity vector ($m\,s^{-1}$)
U_{cell}	cell voltage (V)
$\bar{V}_{H_2O}$	specific volume of water ($m^3\,mol^{-1}$)
$\bar{V}_M$	specific volume of dry membrane ($m^3\,mol^{-1}$)
w	mass fraction
x	mole fraction

Greeks

α	symmetry factor
γ	transport parameter ($mol^2\,m^{-1}\,s^{-1}\,J^{-1}$)
ϵ	effectiveness factor
η	dynamic gas viscosity (Pa s)
η	overvoltage (V)
κ	permeability (m^2)
λ	water content
μ	chemical potential ($J\,mol^{-1}$)
ξ	electroosmotic drag coefficient
ρ	density ($kg\,m^{-3}$)
σ	electric conductivity ($S\,m^{-1}$)
ψ	permeation coefficient ($mol\,s^{-1}\,m^{-1}\,Pa$)
φ	electric potential (V)

Superscripts and subscripts

00	equilibrium potential at standard conditions
A	anode
ag	agglomerate
C	cathode
C	carbon
drag	water transport due to electroosmotic drag
eq	equilibrium
H^+	protons
Kn	Knudsen
M	membrane
P	protons
Pt	platinum
ref	reference state
s	solid phase

normal fuel cell. Because of the fast reaction kinetics, the anode potential is approximately $\varphi_A \approx 0$ V while the cathode potential is $\varphi_C \approx 1$ V, each with respect to the membrane. Due to the high in-plane conductivity of the gas diffusion layers and bipolar plates, the electrodes can be regarded as an equipotential surface along the whole cell. The high electrode conductivity in combination with the low membrane conductivity causes a membrane potential drop in the hydrogen starved region, resulting in high cathode potential $\varphi_C > 1$ V. Thus, in the rear part of the cell, anodic reactions are taking place at the cathode catalyst layer and vice versa resulting in a reverse current. Carbon corrosion, water electrolysis and platinum dissolution occur at the cathode side leading to irreversible cell degradation. Note that there is no external driving force necessary for this mechanism and it is not detectable by measuring the cell voltage.

Meyers and Darling [2] presented a 1D-PEMFC model for the simulation of hydrogen starvation conditions. The numerical results support the theory of a membrane potential drop in the hydrogen starved region. Reiser et al. [3] analysed the RCD-mechanism by an experimental setup of two electronically connected fuel cells, where the anode of the first cell is fed with hydrogen and the latter fed with oxygen. Tang et al. [6] conducted experiments where the anode gas is switched between fuel and air repeatedly. Both authors report severe degradation of the cathode catalyst layer resulting in a significant reduction of its thickness. Liu et al. [8] analysed the current density distribution under local hydrogen starvation. They discovered that while the current density in the starved region drops to zero, the cell performance of the non-starved part is not influenced.

In the present work, we build up a steady state 2D-PEMFC model for the simulation of degradation mechanisms when the fuel gas is diluted by nitrogen. We account for carbon corrosion and water electrolysis as undesired side reactions. Platinum dissolution will be considered in a further publication. The two-dimensional approach allows to analyse the interaction of different cell properties (local water content, gas concentration, membrane permeability, gas humidity) on the cell degradation. The final target is to consider all possible starvation conditions in order to evaluate cell degradation under various operation conditions.

2. Mathematical model

In this section, our stationary and isothermal 2D-model of a single PEM fuel cell is presented. The cell is modelled along the channel and in through-plane direction. Fig. 2 shows the model geometry. The picture illustrates a cross-section through the layers of a PEMFC. Anode and cathode consist of a gas channel, a gas diffusion layer and a catalyst layer, respectively, separated by a membrane in between. In the following, each layer of the geometry is called a domain. Gases are flowing from left to right, while the anode is fed with hydrogen and the cathode with air (21% oxygen and 79% nitrogen). The following basic model assumptions are made:

- All gases obey the ideal gas law.
- Gas flow is laminar due to small Reynolds numbers ($Re < 500$).
- Water is always in a gaseous state (i.e., there is no liquid phase).
- The gas mixture consists of five species, namely H_2, O_2, H_2O, CO_2 and N_2.
- The relative humidity of the anode and cathode inlet gas is 95% and 50%, respectively.

The following subsections describe the governing equations. Values for constants and parameters are given in Table 2.

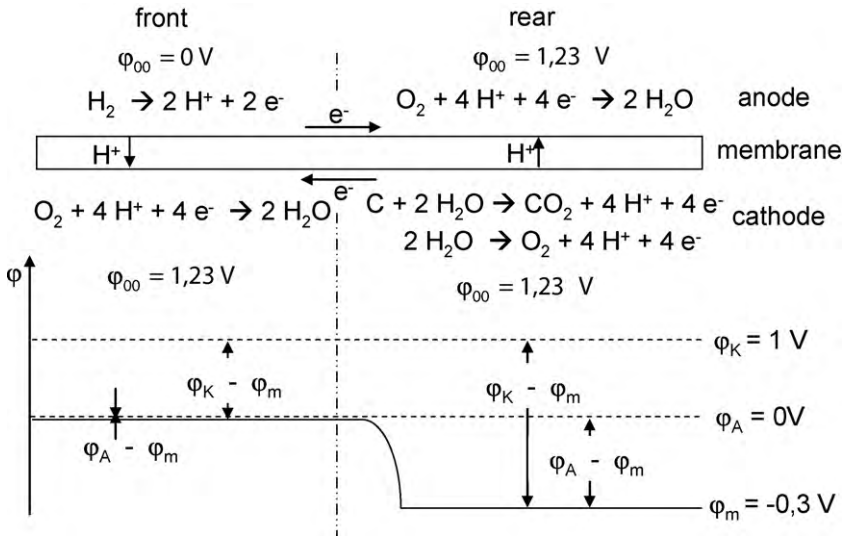

Fig. 1. Reverse current decay mechanism at local hydrogen starvation in the rear part of a PEM cell.

2.1. Mass transport and balancing

The gas flow inside the porous media is described by Darcy's law [9] and the gas transport within the channels is assumed to be a viscous plug-flow. Thus, the mean gas velocity is proportional to the pressure drop:

$$\bar{\mathbf{u}} = -\frac{\kappa}{\eta} \cdot \nabla p \tag{5}$$

where $\bar{\mathbf{u}} = (u, v)^T$ is the average gas velocity, κ the permeability of the porous media, η the dynamic gas viscosity and p the total pressure. Eq. (5) is solved on all domains besides the membrane while the pressure drop is fixed at the inlet and outlet as boundary condition.

The mass transport occurs due to diffusion and convection. As the partial pressure of all gas species (except CO_2) are in the same order of magnitude, interactions of all components are expected to be relevant. The diffusive transport is therefore modelled by a Maxwell–Stefan approach resulting in the following transport equation solved for each species [10]:

$$\nabla \cdot \left(\underbrace{-\rho w_i \sum_{\substack{k=1 \\ k \neq i}}^{N} \tilde{D}_{i,k} \left(\nabla x_k + (x_k - w_k) \frac{\nabla p}{p} \right)}_{\text{diffusion}} + \underbrace{\rho w_i \bar{\mathbf{u}}}_{\text{convection}} \right) = R_i \tag{6}$$

where ρ is the density of the gas mixture, w_k and x_k are mass and mole fraction of species k, $\tilde{D}_{i,j}$ is the inverted Maxwell–Stefan diffusion coefficient matrix and R_i is a source term. The first term on the left hand side represents the diffusive transport (its derivation is given in Ref. [18]) while the latter term describes the convective transport. Eq. (6) is solved on all anode and cathode domains.

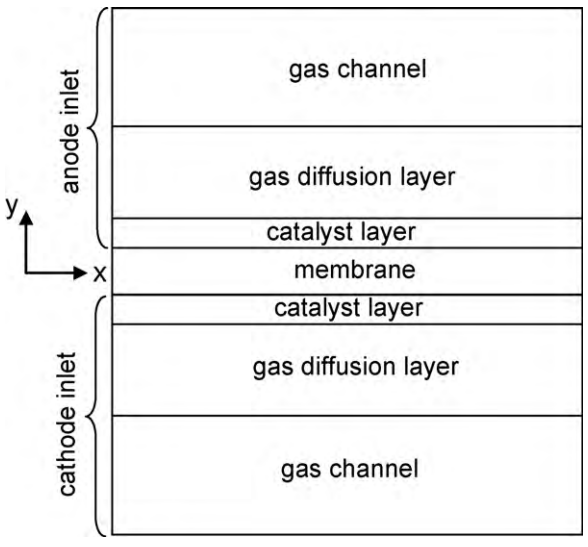

Fig. 2. Geometry of the 2D-PEMFC model.

2.2. Electric conductivity

The electric conductivity of the electrodes (solid phase) is modelled by Ohm's law [11]:

$$i = \sigma_s \nabla \varphi_s \tag{7}$$

where i is the current density, σ_s the electric conductivity and φ_s the electric potential of the solid phase. The cell is operated potentiostatically by fixing the electrode potential at the upper and lower edge of the model geometry (see Fig. 2). Eq. (7) is solved on all domains except for the membrane.

2.3. Membrane

The membrane is modelled according to an approach of Weber and Newman [13]. They derived two model equations for the transport of protons and water molecules in the membrane phase, respectively:

$$i_P = -\sigma_M \nabla \varphi_M - \frac{\sigma_M \xi}{F} \nabla \mu_{H_2O} \tag{8}$$

$$N_{H_2O} = \frac{\sigma_M \xi}{F} \nabla \varphi_M - \left(\gamma + \frac{\sigma_M \xi^2}{F} \right) \nabla \mu_{H_2O} \tag{9}$$

where i_P is the current density of protons and N_{H_2O} the flux density of water molecules within the membrane. φ_M is the membrane

Table 1
Coefficients k_i for the empiric correlation between activity and water content in the membrane [22].

Activity, a_{H_2O}	Temperature (°C)	k_0	k_1	k_2	k_3
$a_{H_2O} \leq 1$	80	0.30	10.80	−16.00	14.10
$1 < a_{H_2O} \leq 2.5$	80	−30.41	61.98	−25.96	3.70

potential, μ_{H_2O} the chemical potential of water in membrane phase, σ_M the ionic conductivity of the membrane, ξ the electroosmotic drag coefficient, γ a transport coefficient and F the Faraday constant.

According to Eqs. (8) and (9), the flux of protons and water molecules is coupled, since both are dependent on the gradient of the electric and the chemical potential. In other words, the approach allows for water transport due to the electroosmotic drag (from the anode to the cathode side) [20] and due to a concentration gradient (back diffusion from the cathode to the anode side because of a high concentration of water in the cathode catalyst layer). Protons are transported due to the electric field as well, but also (coupled to the water flux) due to a gradient in the chemical potential.

The electroosmotic drag coefficient ξ is defined as the number of transported water molecules per proton, when there is no gradient in the water concentration present:

$$\xi = \frac{N_{H_2O}^{drag}}{N_{H^+}} \tag{10}$$

According to an experimental study of Zawodzinski et al. [19], the electroosmotic drag coefficient has the value $\xi = 1$ if the membrane is in equilibrium with water vapor.

Based on the chemical potential μ_{H_2O}, it is possible to determine the local water content λ, which is defined as the number of water molecules per sulfonic acid groups in the Nafion matrix [14]:

$$\lambda = \frac{\text{number of } H_2O - \text{molecules}}{\text{number of } SO_3^- - \text{groups}} \tag{11}$$

Dannenberg et al. [22] propose an empiric correlation between the activity a_{H_2O} and the water content λ:

$$\mu_{H_2O} - \mu_{H_2O}^{ref} = RT \ln a_{H_2O} \tag{12}$$

$$\lambda = k_0 + k_1 a_{H_2O} + k_2 a_{H_2O}^2 + k_3 a_{H_2O}^3 \tag{13}$$

R is the ideal gas constant and T is the cell temperature. The reference potential $\mu_{H_2O}^{ref}$ is set to zero and the coefficients k_i are given in Table 1. Based on the water content λ, the volume fraction f of water within the membrane can be calculated [13]:

$$f = \frac{\lambda \bar{V}_{H_2O}}{\bar{V}_M + \lambda \bar{V}_{H_2O}} \tag{14}$$

where $\bar{V}_{H_2O}$ and $\bar{V}_M$ are the partial molar volume of water and the dry membrane, respectively. The ionic conductivity of the membrane is dependent on its water content [13]:

$$\sigma_M = 200 \cdot (f - 0.06)^{1.5} \tag{15}$$

With respect to the correlation given by Weber and Newman, the prefactor in Eq. (15) has been increased in order to fit the numerical results to experimental data.

The transport parameter γ from Eq. (9) relates the diffusive water flux to the gradient in the chemical potential [21]:

$$\gamma = \frac{c_{H_2O} D_{H_2O}}{RT(1 - x_{H_2O})} \tag{16}$$

R is the ideal gas constant and T is the cell temperature. The local diffusion coefficient D_{H_2O}, the concentration c_{H_2O} and the mole fraction x_{H_2O} of water within the membrane can be calculated by [13]:

Table 2
Constants and parameters.

Name	Symbol	Value	Unit	Reference
Viscosity				
Anode gas	η_A	8.81	μPa s	[24]
Cathode gas	η_C	19.5	μPa s	[24]
Electric conductivity				
Channel	σ_{ch}	5988	S m^{-1}	[23]
GDL/catalyst	$\sigma_{(GDL,cat)}$	71,430	S m^{-1}	[23]
Electroosmotic coefficient	ξ	1	–	[19]
Molar volume of dry membrane	$\bar{V}_M$	5×10^{-4}	m^3 mol^{-1}	[13]
Specific volume of water	$\bar{V}_{H_2O}$	1.8×10^{-5}	m^3 mol^{-1}	
Electrons involved in reaction	n_{H_2}	2	–	
	n_{O_2}	4	–	
	n_C	2	–	
Exchange current density	$i_{H_2} \cdot A_{Pt}$	2.8×10^8	A m^{-3}	Fitted
	$i_{O_2} \cdot A_{Pt}$	2.8×10^4	A m^{-3}	Fitted
	$i_C \cdot A_C$	7.2×10^{-11}	A m^{-3}	[3]
Agglomerate radius	R_{agg}	1×10^{-7}	m	
Diffusion coefficient	$D_{H_2,Kn}$	1.3×10^{-5}	m^2 s^{-1}	[21]
	$D_{O_2,Kn}$	3.2×10^{-7}	m^2 s^{-1}	[21]
Faraday constant	F	96,485	C mol^{-1}	
Ideal gas constant	R	8.314	J (mol K)$^{-1}$	

$$D_{H_2O} = 1.8 \times 10^{-5} \cdot f \tag{17}$$

$$c_{H_2O} = \frac{\lambda}{\bar{V}_{H_2O}\,\lambda +, \bar{V}_M} \tag{18}$$

$$x_{H_2O} = \frac{\lambda}{\lambda + 1} \tag{19}$$

The membrane transport Eqs. (8) and (9) are solved for both catalyst layers and the membrane domain. The catalyst layer is therefore assumed to be a homogeneous mixture of solid phase (electrodes), membrane phase (Nafion) and gas phase.

2.4. Gas permeation

Even though one function of the membrane in the fuel cell is to separate the anode and cathode gas domains, it is not completely gas-tight. A small amount of hydrogen, oxygen and nitrogen is permeating through the membrane to the opposite catalyst layer. If the anode is locally starved of hydrogen, oxygen permeation leads to the RCD-mechanism (see Fig. 1 in Section 1). The permeation flux N_i^p of species i is described by

$$N_i^p = \psi_i \nabla p_i \tag{20}$$

where p_i is the partial pressure of species i. The permeation coefficient ψ_i can be interpreted as the product of Henry's coefficient and Fick's diffusion coefficient. The permeability of the membrane is dependent on its water content. Assuming equilibrium between membrane and the saturated gas phase, Ahluwalia and Wang [15] propose the following expressions for the permeation coefficients:

$$\psi_{H_2} = (0.29 + 2.2f) \times 10^{-11} \exp\left[\frac{E_{H_2}}{R}\left(\frac{1}{T_{ref}} - \frac{1}{T}\right)\right] \tag{21}$$

$$\psi_{O_2} = (0.11 + 1.9f) \times 10^{-11} \exp\left[\frac{E_{O_2}}{R}\left(\frac{1}{T_{ref}} - \frac{1}{T}\right)\right] \tag{22}$$

$$\psi_{N_2} = (0.0295 + 1.21f - 1.93f^2) \times 10^{-11} \exp\left[\frac{E_{N_2}}{R}\left(\frac{1}{T_{ref}} - \frac{1}{T}\right)\right] \tag{23}$$

where $E_{H_2} = 21\,\mathrm{kJ\,mol^{-1}}$, $E_{O_2} = 22\,\mathrm{kJ\,mol^{-1}}$, $E_{N_2} = 24\,\mathrm{kJ\,mol^{-1}}$ and $T_{ref} = 303\,\mathrm{K}$. T is the cell temperature, R is the ideal gas constant and f is the volume fraction of water within the membrane (see Eq. (14)). The transport of water through the membrane is already considered in Eq. (9) and the permeation of carbon dioxide is negligible due to its very low concentrations. Eq. (20) is solved on both catalyst layers and the membrane domain.

2.5. Electrochemical reactions

The electrochemical reactions of hydrogen (Eq. (1)) and oxygen (Eq. (2)) are modeled by Butler–Volmer equations:

$$i_{H_2} = A_{Pt}\, i^0_{H_2}\, x_{H_2} \left[\exp\left(\frac{\alpha_{H_2}\, n_{H_2}\, F}{RT}\, \eta_{H_2} \right) - \exp\left(-\frac{(1-\alpha_{H_2})\, n_{H_2}\, F}{RT}\, \eta_{H_2} \right) \right] \quad (24)$$

$$i_{O_2} = A_{Pt}\, i^0_{O_2}\, x_{O_2} \left[\exp\left(\frac{\alpha_{O_2}\, n_{O_2}\, F}{RT}\, \eta_{O_2} \right) - \exp\left(-\frac{(1-\alpha_{O_2})\, n_{O_2}\, F}{RT}\, \eta_{O_2} \right) \right] \quad (25)$$

while the carbon corrosion reaction (Eq. (3)) is modelled by a simplified Butler–Volmer approach proposed by Reiser et al. [3]:

$$i_C = A_C\, i^0_C \cdot \exp\left(\frac{\alpha_C\, n_C\, F}{RT}\, \eta_C \right) \quad (26)$$

i^0_i is the exchange current density, n_i is the number of electrons involved in the electrode reaction and α_i is the symmetry factor of the corresponding reaction. T is the cell temperature, F is the Faraday constant and R is the ideal gas constant. A_{Pt} and A_C are the surface area of platinum and carbon per volume unit of catalyst layer, respectively.

The overpotential η_i is defined as the difference between the electrode potential φ_S, the membrane potential φ_M and the equilibrium potential φ^{eq}_i of the relevant reaction:

$$\eta_i = \varphi_S - \varphi_M - \varphi^{eq}_i \quad (27)$$

It can been seen from Eq. (26) that only the anodic part of the carbon corrosion reaction is considered. This is reasonable since the reaction product CO_2 leaves the cell with the gas flow. Thus, the back reaction can be neglected. Furthermore, it should be noted that water electrolysis is the back reaction of the oxygen reduction (see Eq. (2)). If the potential difference between electrode and membrane is >1.23 V the overpotential η_{O_2} becomes positive and the first exponential term of Eq. (25) dominates the reaction rate. Eq. (25) therefore describes both oxygen reduction and water electrolysis depending on its sign. All electrochemical reactions are implemented in both catalyst layers. Thus, it is also accounted for the conversion of permeated oxygen and hydrogen.

As an advancement to the standard Butler–Volmer expressions, the electrochemical reactions of hydrogen and oxygen are also described by the agglomerate model proposed by Jaouen et al. [16]. In this approach it is assumed that the catalyst layer is composed of spherical agglomerates consisting of single carbon particles (see Fig. 3). The electrochemical reaction of hydrogen and oxygen occurs within the agglomerates at the active platinum surface area. Both the composite of agglomerates and the agglomerate

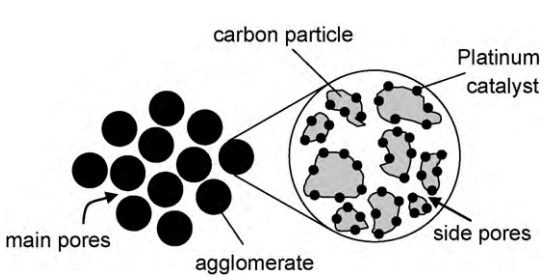

Fig. 3. Structure of catalyst layer containing carbon agglomerates.

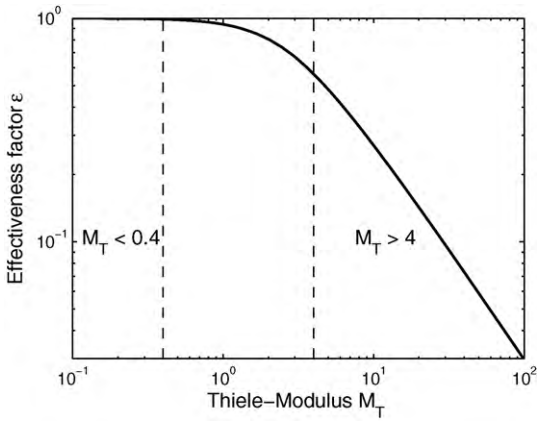

Fig. 4. The effectiveness factor ϵ as function of the Thiele-Modulus M_T.

itself are porous, containing *main pores* in between and *side pores* within the agglomerates. The reactant gases have to diffuse into the catalyst layer through the main pores and subsequently into the agglomerates through the side pores in order to react at the catalyst surface area. The diffusion into the agglomerates represents an additional transport resistance. According to Jaouen et al. [16], the average reaction rate within an agglomerate can be calculated from the gas concentration in the main pores under consideration of the effectiveness factor ϵ. It states the reduction of the mean reaction rate due to the diffusion resistance within the agglomerate.

$$i^{ag}_i = i_i \cdot \epsilon = i_i \cdot 3\, \frac{1 - M_T \cdot \coth M_T}{M_{T^2}} \quad (28)$$

i_i is the current density according to the standard Butler–Volmer expression (Eq. (24) or (25)) and i^{ag}_i is the average current density within the agglomerates. The expression for the effectiveness factor ϵ is derived in Appendix A. It contains the so-called Thiele-Modulus M_T [17]:

$$M_T = R_{agg} \sqrt{\frac{k_i}{D_{i,Kn}}} \quad (29)$$

$$\text{where} \quad k_i = \frac{A_{Pt}\, i^0_i}{c^{ref}_i\, n_i\, F} \cdot \left\{ \left| \exp\left(\frac{n_i\, \alpha_i\, F}{RT}\, \eta_i \right) - \exp\left(\frac{n_i\, (1-\alpha_i)\, F}{RT}\, \eta_i \right) \right| \right\} \quad (30)$$

R_{agg} is the agglomerate radius, k_i is the reaction constant, $D_{i,Kn}$ is the Knudsen diffusion coefficient and c^{ref}_i is a reference concentration of species i. The other parameters match the Butler–Volmer approach. Fig. 4 shows the effectiveness factor ϵ as a function of the Thiele-Modulus M_T. For $M_T < 0.4$ we optain $\epsilon \approx 1$ representing negligible diffusion resistance and therefore conformance with the standard Butler–Volmer expression. This can be reasoned with a small agglomerate radius R_{agg}, a small reaction constant k_i or a large diffusion coefficient $D_{i,Kn}$. For $M_T > 4$ the value of ϵ decreases exponentially. This can be explained with a large agglomerate radius R_{agg}, a large reaction constant k_i or a small diffusion coefficient $D_{i,Kn}$.

By comparison of the numerical results using the Butler–Volmer and the agglomerate approach it should be analysed if the use of the more complex agglomerate model is necessary for a given real fuel cell.

2.6. Software

The mathematical model is implemented using the commercial software COMSOL Multiphysics 3.5. Eqs. (5)–(7) and (20) are implemented using its chemical engineering module. Eqs. (8) and (9) are implemented using the coefficient form of a partial differential

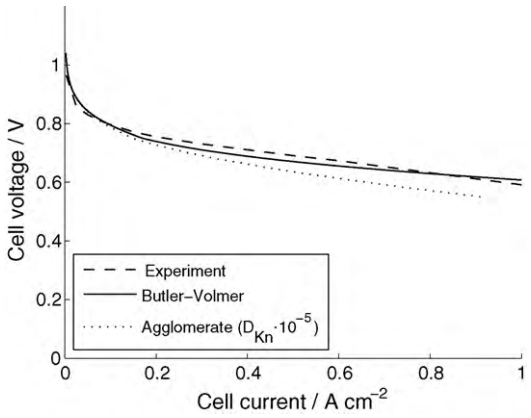

Fig. 5. Experimental and numerical polarisation curves. The curve for the agglomerate model using standard parameters is identical with the Butler–Volmer approach.

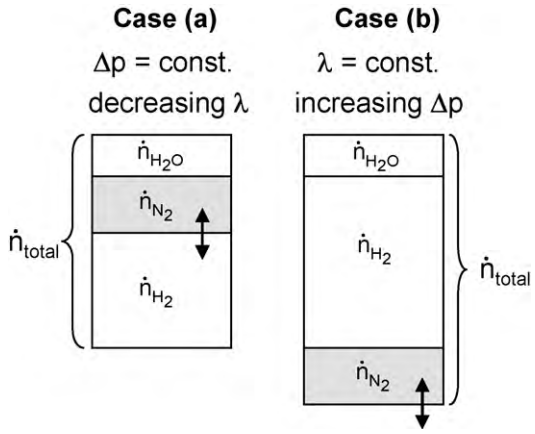

Fig. 6. Hydrogen starvation scenarios: case (a) constant pressure drop and case (b) constant stoichiometry.

equation (PDE) and the Butler–Volmer Eqs. (24)–(26) are implemented as subdomain expressions. The software is suitable for systems containing several physical phenomena that are strongly coupled. The numerical solution of the PDE system is based on the finite element method (FEM).

3. Results and discussion

3.1. Standard conditions

The model behaviour under standard conditions (p = 2.5 bar, T = 348 K, relative humidity $rH_{anode/cathode}$ = 95 / 50%, anode fed with hydrogen and cathode with air) is analysed by the simulation of polarisation curves. The numerical results for the Butler–Volmer and the agglomerate model (see Section 2.5) compared with experimental data of a commercial fuel cell stack is presented in Fig. 5. The Butler–Volmer approach fits the experimental data quite well. The model slightly overestimates the activation losses (i < 0.3 A cm^{-2}) and slightly underestimates the Ohmic resistance (i > 0.3 A cm^{-2}) of the real cell.

Applying the agglomerate model using standard parameters, the numerical polarisation curve is identical with the Butler–Volmer model. Thus, mass transport resistance within the agglomerates is not a limiting factor with respect to the cell performance (i.e., the effectiveness factor is $\epsilon \approx 1$). In order to analyse the effect of strong diffusion resistance within the agglomerates, further simulations with a reduced diffusion coefficient $D_{i,Kn}$ and therefore increased Thiele-Modulus M_T (see Eq. (29) and Fig. 4) are conducted. Fig. 5 shows the polarisation curve of the agglomerate model applying a diffusion coefficient reduced by the factor 10^{-5}. It can be seen that the shape is identical for small current densities (i < 0.2 A cm^{-2}) while there are significant additional Ohmic losses for high current densities. These additional Ohmic losses are due to the limited gas transport inside the agglomerates.

Since the more complex agglomerate model yields no better results, we use the Butler–Volmer approach in order to analyse hydrogen starvation conditions due to its simplicity.

3.2. Hydrogen starvation

Stationary hydrogen starvation conditions are analysed by the consideration of two different cases (see Fig. 6). In case (a), the total anode pressure drop is kept constant while hydrogen is partially replaced by nitrogen. The anode stoichiometry therefore decreases with increasing nitrogen mole fraction. In case (b), the anode stoichiometry is kept constant at λ = 1.6 while the fuel gas is diluted by nitrogen. The more nitrogen is added, the higher is the pressure drop and the total anode gas flow rate.

Considering a real fuel cell system containing an anode gas recycle loop, these two alternatives represent limiting cases. In general, the H_2-consumption (proportional to the cell current) is refilled by fresh hydrogen from the gas tank. While the anode gas is looped, nitrogen enriches due to permeation through the membrane from the cathode side. Until the anode gas is purged, the total flow rate and the pressure drop increase while the stoichiometry is kept constant matching case (b) in Fig. 6.

Since the anode pressure drop is limited by the capacity of the recycle pump, there is a maximum anode gas flow rate. If it is reached, it is no longer possible to refill the entire H_2-consumption by fresh hydrogen due to the steady permeation flux of nitrogen from cathode to anode. This matches case (a) in Fig. 6 as the remaining hydrogen is consumed and the stoichiometry decreases. In order to analyse which case is more critical with respect to the cell degradation, both scenarios are examined.

3.2.1. Case (a) constant pressure drop

Starting with hydrogen at 95% relative humidity, the anode inlet mole fraction $x^{in}_{H_2,A}$ is gradually decreased while hydrogen is replaced by nitrogen. Fig. 7 shows the shape of the local membrane potential φ_M along the cell length depending on the nitrogen inlet concentration at a cell voltage of U_{cell} = 0.7 V. The upper curve representing standard conditions ($x^{in}_{H_2,A} = 0.85$) is slightly increasing because of a decreasing reaction rate and therefore smaller overpotential η (see Eq. (27)) in the rear part of the cell due to reduced reactant gas concentrations. For $x^{in}_{N_2,A} \leq 32\%$, the shape of

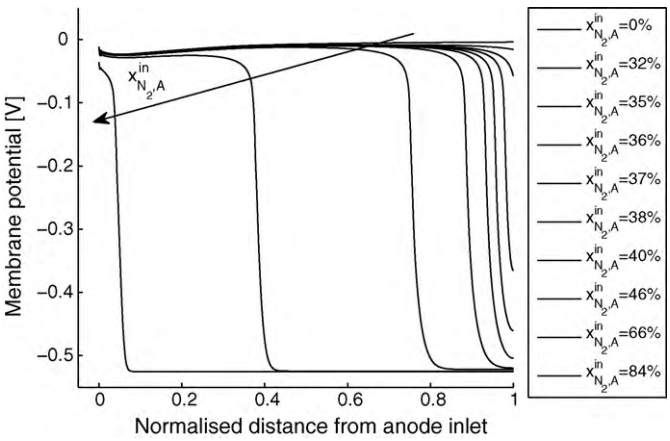

Fig. 7. Plot of the membrane potential φ_M along the cell at U_{cell} = 0.7 V for different nitrogen anode inlet mole fractions.

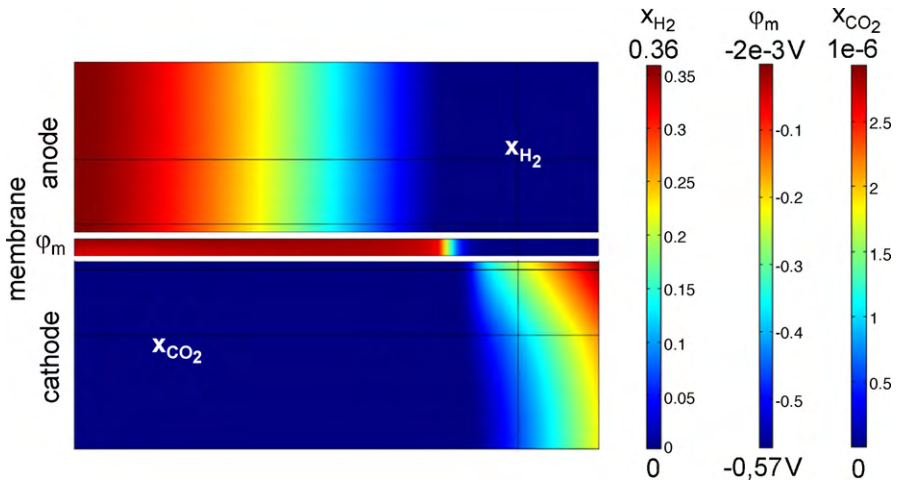

Fig. 8. Local distribution of the hydrogen mole fraction x_{H_2} on the anode, the membrane potential φ_M on the membrane and the carbon dioxide mole fraction x_{CO_2} on the cathode for $x^{in}_{N_2,A} = 0.46$.

the membrane potential shows minor deviations from the standard conditions. If the hydrogen inlet concentration is reduced further, there is a significant membrane potential drop close to the cell outlet.

For $x^{in}_{N_2,A} \geq 40\%$, the membrane potential drops to a minimum value of $\varphi^{min}_M = -0.54\,V$ and for $x^{in}_{N_2,A} \geq 84\%$ it is constant at its minimum almost along the whole cell. The membrane potential drop can be explained by the RCD-mechanism in the hydrogen starved region of the cell (see Section 1). The more hydrogen is replaced by nitrogen, the closer the position of $x_{H_2} = 0$ is moving towards the cell inlet.

Fig. 8 shows the local distribution of the hydrogen mole fraction on the anode, the membrane potential on the membrane and the carbon dioxide mole fraction on the cathode at a nitrogen inlet mole fraction of $x^{in}_{N_2,A} = 46\%$. In Fig. 8, red colour represents high values and blue colour low values of mole fraction and potential, respectively. The hydrogen mole fraction decreases and reaches $x_{H_2} = 0$ at about half of the cell length. At this point, the membrane potential drops down to its minimum value and a significant production of carbon dioxide at the cathode can be observed. As the cathode potential is fixed to $\varphi_C = 0.7\,V$, the cathodic potential difference between electrode and membrane reaches $\Delta\varphi = 1.24\,V$ in the hydrogen starved region. The high cathode potential relative to the membrane leads to a significant carbon corrosion reaction rate and also water electrolysis. The current flow direction has changed in the rear part of the cell as there are anodic reactions at the cathode (corrosion and electrolysis) and cathodic reactions at the anode (reduction of permeated oxygen).

Regarding Fig. 7, it is noticeable that the membrane potential drops to a constant minimum under hydrogen starvation. This can be explained by the coupling of carbon corrosion/water electrolysis at the cathode and oxygen reduction at the anode due to the proton transport through the membrane (see Fig. 1). The available amount of oxygen in the anode catalyst layer is the limiting factor for the RCD-mechanism because oxygen is transported to the anode only by permeation through the membrane from the cathode side. In order to support that assumption, further simulations are conducted varying the O_2 permeation coefficient and thereby the amount of permeated oxygen. In Fig. 9, the shape of the membrane potential in the hydrogen starved region is plotted depending on the oxygen permeation coefficient. At standard conditions it has a value of $\psi_{O_2} \approx 2 \times 10^{-14}\,mol\,(s\,m\,Pa)^{-1}$.

The diagram shows that the minimum membrane potential drops on a lower level if the permeation coefficient is increased and vice versa. The RCD-mechanism at local starvation is therefore influenced by the amount of oxygen available in the anode catalyst layer. Considering the present example, a difference in the minimum membrane potential of $\Delta\varphi^{min}_M = 16\,mV$ leads to a change of the carbon corrosion reaction rate by a factor of 1.6.

On the left hand side in Fig. 10, the shape of the membrane potential under local hydrogen starvation next to the cell outlet is presented for different cell voltages $U_{cell} = 0.55\,V, \ldots, 1\,V$. It can be seen that lower cell voltages lead to lower membrane potential drops. The right diagram in Fig. 10 shows that there is an almost linear correlation between the cell voltage and the corresponding minimum membrane potential, for example for $U_{cell} = 0.9\,V$ it is $\varphi^{min}_M = -320\,mV$ while for $U_{cell} = 0.6\,V$ it is $\varphi^{min}_M = -610\,mV$. The right diagram also shows that the total potential difference between cathode and membrane is almost constant and independent from the cell voltage. Carbon corrosion and water electrolysis reaction rates are therefore the same throughout the operating conditions $U_{cell} = 0.55\,V, \ldots, 1\,V$. This is reasonable since the oxygen permeation flux through the membrane and therefore its available amount in the H_2-starved part of the cell is constant and independent from the cell voltage. The RCD-mechanism leads to a complete reduction of the available oxygen resulting in similar cell degradation at the cathode side regardless of the cathode potential.

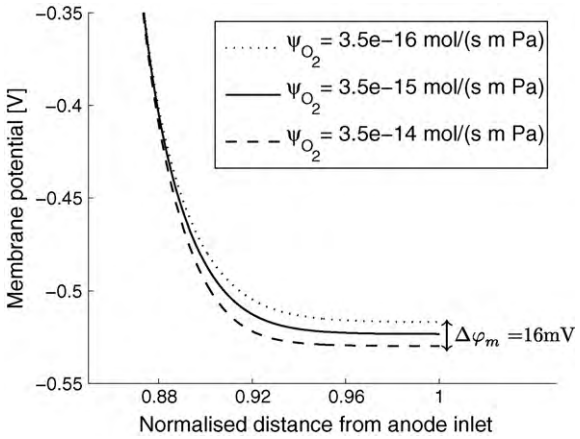

Fig. 9. Shape of the membrane potential φ_M under hydrogen starvation at varying oxygen permeation coefficients.

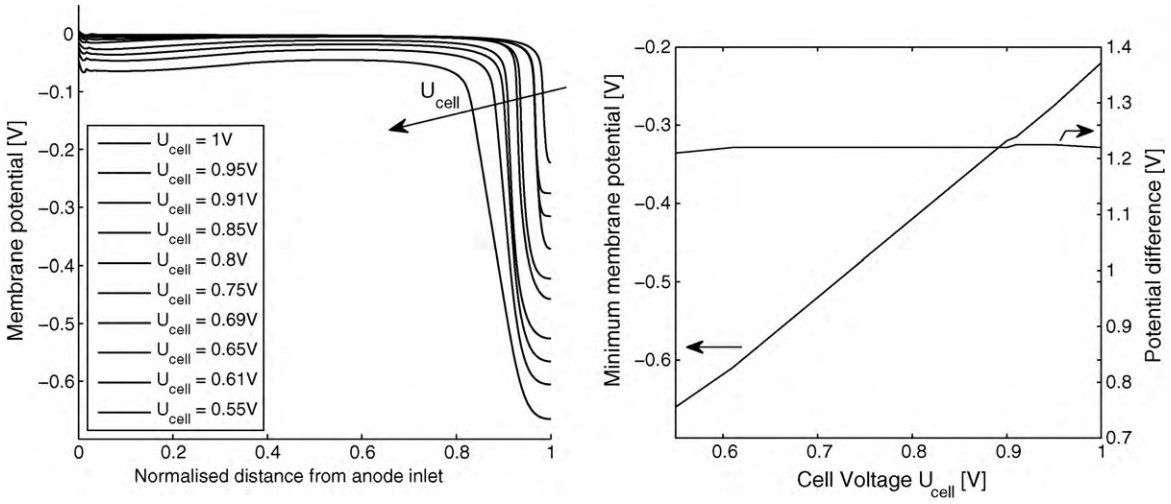

Fig. 10. Left: shape of the membrane potential for varying cell voltage; right: linear correlation between cell voltage and minimum membrane potential resulting in a constant potential difference between cathode and membrane.

3.2.2. Case (b) constant anode stoichiometry

Considering case (b) from Fig. 6, the anode gas is diluted by nitrogen while the stoichiometric factor is kept constant at $\lambda = 1.6$. The anode pressure drop is increased in 100 mbar steps up to a maximum of $\Delta p = 1$ bar. As the cell is run potentiostatically, the global cell current decreases with increasing nitrogen dilution. The hydrogen gas flow rate is therefore lowered while the total anode gas flow is increased in order to keep the stoichiometric factor constant. In Fig. 11, the membrane potential φ_M is plotted for different pressure drops at $U_{cell} = 0.75$ V. It can be seen that φ_M decreases along the whole cell with increasing nitrogen dilution. This is in contrast to case (a), where deviation in the membrane potential is only observed in the hydrogen starved rear part of the cell (compare to Fig. 7). The behaviour under case (b) can be reasoned with low hydrogen concentration and therefore large overpotential when the anode gas is strongly diluted by nitrogen.

Furthermore, the membrane potential is decreasing along the cell length but it does not reach a minimum. Comparing standard conditions and the maximum nitrogen dilution at $\Delta p = 1$ bar (upper and lower curve in Fig. 11), the total membrane potential difference is about 60 mV. Since the cathode potential is fixed to $\varphi_C = 0.75$ V, the total difference between the membrane and the cathode reaches $\Delta\varphi_C \approx 0.81$ V. At these conditions, there is no water electrolysis and carbon corrosion reaction rates are still negligible. This is underlined in the following section.

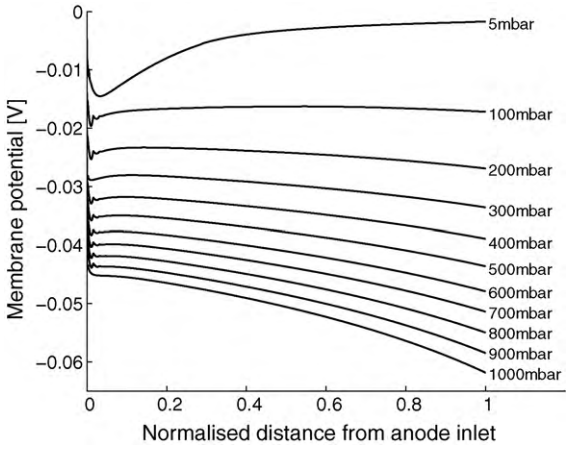

Fig. 11. Local membrane potential for varying pressure drop at constant stoichiometry $\lambda = 1.6$.

3.2.3. Comparison: case (a) vs. case (b)

In this section, the effect of nitrogen dilution at constant pressure drop and at constant stoichiometry is compared. Therefore, the numerical results for a pressure drop of $\Delta p = 300$ mbar (i.e. $\lambda = 1.6$ at $U_{cell} = 0.75$ V, third curve from the top in Fig. 11) are

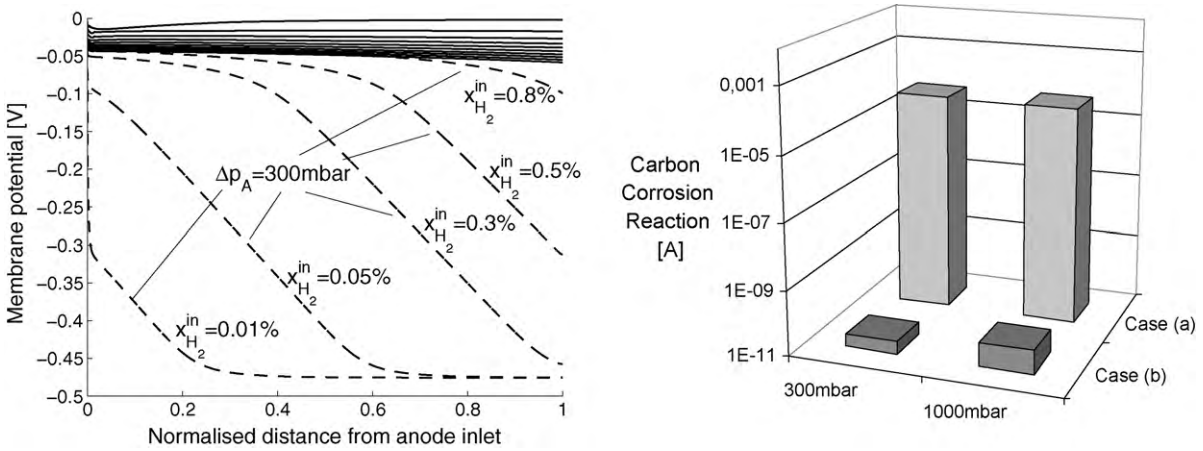

Fig. 12. Left: shape of the local membrane potential comparing case (a) and case (b); right: comparison of corrosion reaction rates at constant pressure drop and at constant stoichiometry.

set as initial conditions. Subsequently, the initial hydrogen anode inlet mole fraction $x_{H_2}^{in} = 1.6\%$ is lowered while the pressure is kept constant. The left diagram in Fig. 12 shows all curves from Fig. 11 (representing case (b)) and the shape of the membrane potential for different values of $x_{H_2}^{in}$ at $\Delta p = 300$ mbar (dashed lines representing case (a)). It can be seen that the membrane potential drops significantly and reaches a constant minimum of $\varphi_M^{min} = -0.48$ V when the total hydrogen gas flow fed to the anode is lowered. As soon as the local hydrogen concentration drops to zero, the RCD-mechanism is established. Note that all dashed lines in Fig. 12 are at $\lambda = 1$ since the total cell current decreases with decreasing hydrogen inlet mole fraction and all H_2 is consumed. The right diagram in Fig. 12 gives the total current density due to carbon corrosion in the cathode catalyst layer for case (a) and (b) at an anode pressure drop of 300 and 1000 mbar, respectively. Considering constant stoichiometry ($\lambda = 1.6$, case (b)), the carbon corrosion reaction rate increases with increasing pressure drop. However, its value is negligible compared to carbon corrosion at constant pressure drop (case (a)) and decreasing stoichiometry down to $\lambda = 1$ (note the logarithmic scale at the y-axis).

4. Conclusion

In this study we have built up a 2D-PEMFC model that includes carbon corrosion and water electrolysis reactions. Regarding standard conditions, the numerical polarisation curve applying standard Butler–Volmer expressions for the electrochemical reactions fits the experimental data quite well. The implementation of the more complex agglomerate model yields no better results. Hydrogen starvation conditions are therefore only simulated using the Butler–Volmer model.

Regarding hydrogen starvation condition, the model supports the theory of a reverse current decay mechanism [3]. If the local hydrogen concentration drops down to $c_{H_2} = 0$, the model predicts a membrane potential drop leading to high cathode potentials $\varphi_C > 1$ V with respect to the membrane. Local carbon corrosion and water electrolysis are observed at the cathode side. The cell degradation is independent of the cell voltage. The limiting factor is the permeation flux of oxygen through the membrane since the undesired side reactions at the cathode side are coupled to the oxygen reduction at the anode side.

In a continuative study, we will build up a transient model in order to analyse start-up and shut-down procedures. Furthermore, platinum dissolution will be included as an additional undesired side reaction and the cell will be operated both potentiostatically and galvanostatically. The final aim is to investigate all possible starvation conditions in order to evaluate cell degradation under various operating conditions.

Appendix A. Agglomerate model

Considering a spherical shell of thickness Δr within an agglomerate, the mass balance for species A yields the following diffential equation [21]:

$$D_A \frac{1}{r^2} \frac{d}{dr}\left(r^2 \frac{dc_A}{dr}\right) = k c_A \tag{A.1}$$

r is the agglomerate radius, k is the reaction constant, D_A is the Fick's diffusion coefficient and c_A is the concentration of species A within the agglomerate.

The following boundary conditions are applied:

(i) $c_A = c_A^0 \quad \text{for } r = R$

(ii) $\frac{dc_A}{dr} = 0 \quad \text{for } r = 0$

c_A^0 is the concentration at the agglomerate surface area (within the main pores). Integration over the agglomerate radius leads to the following expression for the concentration of species A within the agglomerate:

$$c_A = c_A^0 \frac{R}{r} \frac{\sinh(\sqrt{(k/D)}\, r)}{\sinh(\sqrt{(k/D)}\, R)} \tag{A.2}$$

The reactant gas consumption rate is determined by:

$$N_A^{reac} = -D_A \cdot \left.\frac{dc_A}{dr}\right|_{r=R} \cdot 4\pi R^2 \tag{A.3}$$

$$= 4\pi R c_A^0 D_A \left(1 - \sqrt{\frac{k}{D_A}} R \cdot \coth\sqrt{\frac{k}{D_A}} R\right) \tag{A.4}$$

If the diffusion resistance is neglected, the reactant gas consumption is

$$N_A^{reac,0} = \frac{4}{3}\pi R^3 \cdot k c_A^0 \tag{A.5}$$

The effectiveness factor ϵ is the relationship of the reaction rate with and without diffusion resistance where $0 < \epsilon < 1$:

$$\epsilon = \frac{N_A^{reac,}}{N_A^{reac,0}} = -\frac{3}{M_T^2} \cdot (1 - M_T \coth M_T) \tag{A.6}$$

M_T is the Thiele-Modulus

$$M_T = \sqrt{\frac{k}{D_A}} R \tag{A.7}$$

References

[1] G. Milazzo, S. Caroli, Tables of Standard Electrode Potentials, John Wiley & Sons, Chichester, USA, 1978.
[2] J.P. Meyers, R.M. Darling, J. Electrochem. Soc. 153 (2006) A1432–A1442.
[3] C.A. Reiser, L. Bregoli, T.W. Patterson, J.S. Yi, J.D. Yang, M.L. Perry, T.D. Jarvi, Electrochem. Solid-State Lett. 8 (2005) A273–A276.
[4] M. Pourbaix, Atlas of Electrochemical Equilibria in Aqueous Solutions, National Association of Corrosion Engineers, Houston, TX, 1974.
[6] H. Tang, Z. Qi, M. Ramani, J.F. Elter, J. Power Sources 158 (2006) 1306–1312.
[7] R.M. Darling, J.P. Meyers, J. Electrochem. Soc. 150 (2003) A1523–A1527.
[8] Z. Liu, L. Yang, Z. Mao, W. Zhuge, Y. Zhang, L. Wang, J. Power Sources 157 (2006) 166–176.
[9] H. Darcy, Les Fontaines Publiques de la Ville Dijon, Dalmont, Paris, 1856.
[10] C.F. Curtiss, R.B. Bird, Ind. Eng. Chem. Res. 38 (1999) 2515–2522.
[11] G.S. Ohm, Die galvanische Kette, Berlin, 1827.
[13] A.Z. Weber, J. Newman, J. Electrochem. Soc. 150 (2003) A1008–A1015.
[14] J. Fimrite, H. Struchtrup, N. Djilali, J. Electrochem. Soc. 152 (2005) A1804–A1814.
[15] R.K. Ahluwalia, X. Wang, J. Power Sources 171 (2007) 63–71.
[16] F. Jaouen, G. Lindbergh, G. Sundholm, J. Electrochem. Soc. 149 (2002) A437–A447.
[17] O. Levenspiel, Chemical Reaction Engineering, 3rd edition, John Wiley & Sons, Hoboken, USA, 1999, p. 381.
[18] R. Taylor, R. Krishna, Multicomponent Mass Transfer, Wiley Interscience, New York, 1993.
[19] A. Zawodzinski, C. Derouin, S. Radzinski, R.J. Sherman, V.T. Smith, T.E. Springer, S. Gottesfeld, J. Electrochem. Soc. 140 (1993) 1041–1047.
[20] N. Agmon, Chem. Phys. Lett. 244 (1995) 456–462.
[21] R.B. Bird, W.E. Stewart, E.N. Lightfoot, Transport Phenomena, 2nd edition, John Wiley & Sons, New York, 2002.
[22] K. Dannenberg, P. Ekdunge, G. Lindbergh, J. Appl. Electrochem. 30 (2000) 1377–1387.
[23] M. Sundaresan, A thermal model to evaluate sub-freezing startup for a direct hydrogen hybrid fuel cell vehicle polymer electrolyte fuel cell stack and system, Dissertation, University of California, Davis, 2004.
[24] B. Poling, J. Prausnitz, J. O'Connell, The Properties of Gases and Liquids, 5th edition, The McGraw-Hill Companies, Inc., Boston, USA, 2001.